Enhancing Rotation in Quadruped Robots Using Multi-Degree-of-Freedom Tails

R Rajkumar[1], J Stephen Ponraj[1], M Gowtham[1], M Yathish prasanna[1], P Divakaran[1]*

[1]Department of Mechanical Engineering, Nandha Engineering College, Perundurai 638 052, Tamilnadu, India

Abstract: The effects of a robotic tail's planar shape on a quadruped robot's ability to manipulate yaw angles are examined in this research. A quadruped model that takes ground contact friction into consideration is included in the simulation, along with tail structures that vary from a 1-degree of freedom (1 DOF) pendulum to a six-degree-of-freedom serpentine robot. To take advantage of the tail's motion and enhance net quadruped rotation, trajectories are generated utilizing split-cycle frequency modulation. In order to numerically investigate the effect of trajector parameters and tail assembly on the neted quadruped spin, quadruped and tail models are employed. The results demonstrate the value of a multi-DOF tail and stress the significance of centripetal and tangential loads on tail trajectory planning.

1 Introduction

Animals use their tails for stabilization and movement in the wild. In terms of movement, cheetahs can turn their tails while running, geckos can reorient themselves when jumping, and alligators can roll to strike prey more effectively [1]. When it comes to stability, kangaroos utilize their tails as a fifth leg when running, monkeys as a climbing assist, and house cats as a means of maintaining equilibrium. Researchers in the field of robotics have used these findings as a starting point to develop onboard robotic systems that mimic similar structures [2,3] Research in robotics pertaining to structures resembling tails has mostly concentrated on the use of single-degree-of-freedom pendulums for a particular task: controlling the pitch of walking, climbing, yaw angle turning, quick acceleration/ deceleration, and stabilizing disturbances [4]. Research on multi-DOF tails is still in its early stages. In a similar vein, serpentine and continuum robots from the hyper-redundant robotics domain can exhibit several mode configurations and have structures that are essentially similar to biological tails [5,6]. This research examines and contrasts the net quadruped yaw rotation as a function of inertial loading produced by planar tail structures with degrees of freedom ranging from 1 to 6 degrees of freedom. Furthermore, it investigates how different trajectory parameters affect the net rotation of the quadruped [7].

2 Mathematical Model

Here we show the mathematical model of the six-tailed and quadrupedal systems, including their dynamics and kinematics.

2.1 Quadruped and Tail Kinematics

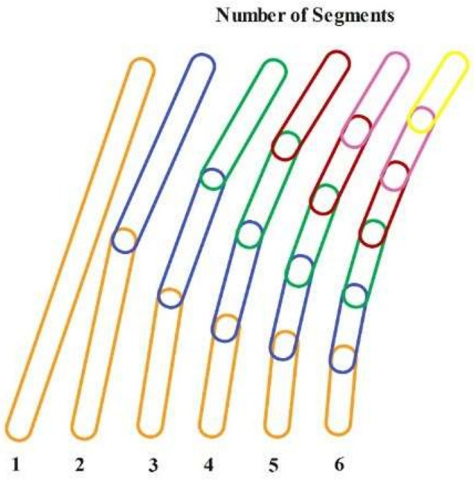

Fig. 1. Degree of freedom - Tail pattern

Figure 1 shows six possible tail structures that are being evaluated for the purpose of studying the effect of tail form on presentation. The 6 Degree of freedom tail attached to the quadruped model that was taken into account in this research. At first, we thought about using a flywheel construction as well, but our early simulations revealed that it performed far worse than pendulum structures. This is because there are no inertial forces produced by the flywheel's applied loading, which is only an instant. Therefore, the imposed load with relation to the system center of mass (COM) remains same irrespective of the flywheel's location; the placement of the flywheel just affects the net system COM's body-fixed position.

* Corresponding Author: rajkumar1229@gmail.com

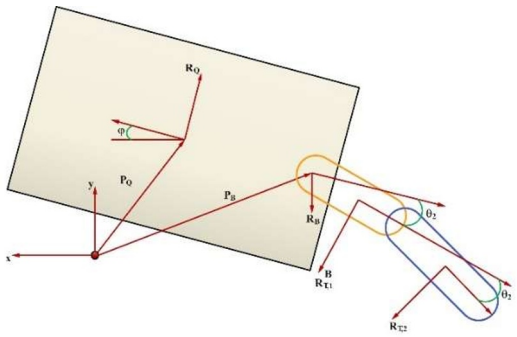

Fig. 2. Coordinates and template frames for a quadruped with 2 DOF tail

The three planar quadruped has three degrees of freedom (DOF) which include translations in the x and y directions and rotation denoted by φ. Equation (1) in the ground frame xyz defines the orientation of the quadruped as $\boldsymbol{R}_Q$ and the orientation of the tail base as $\boldsymbol{R}_B$ [8,9]. The Z-axis rotation matrix for angle γ is denoted by $\boldsymbol{R}_Z(\gamma)$. The tail link orientations, $\boldsymbol{R}^B_{T,i}$, are likewise stated in relation to $\boldsymbol{R}_B$. Vectors or matrices constructed with regard to $\boldsymbol{R}_B$ are indicated with a B superscript.

$$\boldsymbol{R}_Q = \boldsymbol{R}_Z(\varphi), \quad \boldsymbol{R}_B = \boldsymbol{R}_Q\boldsymbol{R}_Z(180\text{deg}), \quad \boldsymbol{R}^B_{T,i} = \begin{cases} \boldsymbol{R}_Z(\theta_i), & i \geq 1 \\ \boldsymbol{R}^B_{T,i-1}\boldsymbol{R}_Z(\theta_i) \end{cases} \tag{1}$$

Equation (2) specifies the position of the quadruped as $\boldsymbol{p}_Q$and the location of the tail base as $\boldsymbol{p}_B$, where d_{Q2B} represents the distance between the quadruped's center of mass and the tail base [10], [11].

$$\boldsymbol{p}_Q = [x \quad y \quad 0]^T, \; \boldsymbol{p}_B = \boldsymbol{p}_Q - d_{Q2B}\boldsymbol{R}_Q\boldsymbol{x} \tag{2}$$

$$\boldsymbol{p}^B_{J,i} = \begin{cases} 0, & i = 1 \\ \boldsymbol{p}^B_{J,i} + L_L\,\boldsymbol{R}^B_{T,i-1}\boldsymbol{x}, & i > 1 \end{cases} \boldsymbol{p}^B_{L,i} = \boldsymbol{p}^B_{J,i} + 0.5\,L_L\boldsymbol{R}^B_{T,i}\boldsymbol{x} \tag{3}$$

$$\omega_Q = \dot{\varphi}\boldsymbol{R}_Q z, \omega^B_{T,i} = \begin{cases} \dot{\theta}_i\boldsymbol{R}^B_{T,i}z, & i = 1 \\ \omega^B_{T,i-1} + \dot{\theta}_i\boldsymbol{R}^B_{T,i}z, & i > 1 \end{cases} \tag{4}$$

Where,

Angular accelerations $\boldsymbol{\alpha}_Q$and $\boldsymbol{\alpha}^B_{T,i}$ with respect to time.

Linear velocity $\boldsymbol{v}^B_{J,i}$, $v^B_{L,i}$

linear acceleration $\boldsymbol{a}^B_{J,i}$, $\boldsymbol{a}^B_{L,i}$

The underlying assumption of tail dynamics is that the tail has an actuation mechanism that can be used to produce the desired tail motion, and that the inertia of the tail completely absorbs the effect of this actuation. The base tail loading is determined by using a recursive.

$\boldsymbol{F}_{J,i}$ Joint forces

$\boldsymbol{M}_{J,i}$ Moments.

$m_{L,i}$ link i mass

$I_{zz,L,i}$ moment of inertia for the link iz-axis

$\tilde{\boldsymbol{p}}\boldsymbol{F}$ $\boldsymbol{p}\times\boldsymbol{F}$.

Equation (8) defines the loading of tail on the quad ($\boldsymbol{F}_B$. and $\boldsymbol{M}_B$) [12], [13]:

$$\boldsymbol{F}^B_{J,i} = \begin{cases} m_{L,i}\boldsymbol{a}^B_{L,i}, & i = n \\ \boldsymbol{F}^B_{J,i+1} + m_{L,i}\boldsymbol{a}^B_{L,i}, & i < n \end{cases} \tag{5}$$

$$\boldsymbol{M}^B_{J,i} = \begin{cases} I_{zz,L,i}\alpha^B_{T,i} - \tilde{\boldsymbol{p}}^B_{L2J,i,i}\boldsymbol{F}^B_{J,i}, & i = n \\ \boldsymbol{M}^B_{J,i+1} + I_{zz,L,i}\alpha^B_{T,i} + \tilde{\boldsymbol{p}}^B_{L2J,i,i+1}\boldsymbol{F}^B_{J,i+1} - \tilde{\boldsymbol{p}}^B_{L2J,i,i}\boldsymbol{F}^B_{J,i}, & i < n \end{cases} \tag{6}$$

$$\boldsymbol{p}^B_{L2J,i,j} = \boldsymbol{p}^B_{J,j} - \boldsymbol{p}^B_{L,i} \tag{7}$$

$$\boldsymbol{F}_B = -\boldsymbol{R}_B\boldsymbol{F}^B_{J,1}, \boldsymbol{M}_B = -\boldsymbol{R}_B\boldsymbol{M}^B_{J,1} \tag{8}$$

The equations governing the quadruped are specified in Eq. (9) [14]

Where,

m mass

I_{zz} z-axis inertia

$\boldsymbol{a}$-COM COM acceleration

$\boldsymbol{F}_T$ and $M_{z,T}$ net tail loading

$\boldsymbol{F}_F$ and $M_{z,F}$ the foot contact friction loading.

p-COMcenter-of-mass position

$$m\boldsymbol{a}_{\text{COM}} = \boldsymbol{F}_T + \boldsymbol{F}_F, \; I_{zz}\ddot{\varphi} = M_{z,T} + M_{z,F} \tag{9}$$

$$m = m_Q + \sum_{i=1}^{n} m_{L,i}$$

$$I_{zz} = I_{zz,Q} + m_Q\|\boldsymbol{p}_{C2Q}\|^2 + \sum_{i=1}^{n}\left(I_{zz,L,i} + m_{L,i}\|\boldsymbol{p}_{C2L,i}\|^2\right) \tag{10}$$

$$\boldsymbol{F}_T = \boldsymbol{F}_B, M_{z,T} = z\cdot\boldsymbol{M}_B + z\cdot(\tilde{\boldsymbol{p}}_B - \tilde{\boldsymbol{p}}_{\text{COM}})\boldsymbol{F}_B \tag{11}$$

$$\boldsymbol{p}_{\text{COM}} = \left(m_Q\boldsymbol{p}_Q + \sum_{i=1}^{n} m_{L,i}\left(\boldsymbol{p}_B + \boldsymbol{R}_B\boldsymbol{p}^B_{L,i}\right)\right)/m \tag{12}$$

$$\boldsymbol{p}_{C2Q} = \boldsymbol{p}_Q - \boldsymbol{p}_{\text{COM}}, \boldsymbol{p}_{C2L,i} = \boldsymbol{p}_B + \boldsymbol{R}_B\boldsymbol{p}^B_{L,i} - \boldsymbol{p}_{\text{COM}} \tag{13}$$

To mimic the static and dynamic friction effects a stiction model is used to denotes the friction loading ($\boldsymbol{F}_F$ and $M_{z,F}$). The magnitudes of the maximal frictional force $F_{F,\max}$ and the moment $M_{z,F,\max}$ can be found using Equation (14) μ_s is the static coefficient of friction μ_d is the dynamic coefficient of friction g is the gravitational acceleration and L_F is the effective friction moment arm [15,16]:

$$F_{F,\max} = \begin{cases} \mu_s mg, \|\boldsymbol{v}_Q\| = 0 \\ \mu_d mg, \|\boldsymbol{v}_Q\| \neq 0 \end{cases}, M_{z,F,max} = \begin{cases} \mu_s mgL_F, \dot{\varphi} = 0 \\ \mu_d mgL_F, \dot{\varphi} \neq 0 \end{cases} \tag{14}$$

The friction loading during translation and rotation is controlled by two variables: the contact velocity and the tail loading. For translation, the variables are $\boldsymbol{v}_Q$ and $\boldsymbol{F}$-T. For rotation, the variables are, φ and M-z, T. For vectors $\hat{\boldsymbol{X}} = \boldsymbol{X}/\|\boldsymbol{X}\|$ and for scalars $\hat{x} = x/|x|$ the values of $\boldsymbol{F}_F$ and $M_{z,F}$ are defined by equations (15) and (16), respectively [17,18].

$$\boldsymbol{F}_F = \begin{cases} -\boldsymbol{F}_T & \|\boldsymbol{v}_Q\| = 0, \|\boldsymbol{F}_T\| < F_{F,\max} \\ -F_{F,\max}\hat{\boldsymbol{F}}_T & \|\boldsymbol{v}_Q\| = 0, \|\boldsymbol{F}_T\| \geq F_{F,\max} \\ -F_{F,\max}\hat{\boldsymbol{v}}_Q & \|\boldsymbol{v}_Q\| \neq 0 \end{cases} \tag{15}$$

$$M_{z,F} = \begin{cases} -M_{z,T} & |\dot{\varphi}| = 0, |M_{z,T}| < F_{F,\max} \\ -M_{F,\max}\hat{M}_{z,T} & |\dot{\varphi}| = 0, |M_{z,T}| \geq F_{F,\max} \\ -M_{F,\max}\hat{\dot{\varphi}} & |\dot{\varphi}| \neq 0 \end{cases} \tag{16}$$

In order to compute O-F it is necessary to have a model of the distribution of contact forces among the four feet of a quadruped. Figure 3 is a top-down quad diagram that shows the four spots (1-4) where the quads' feet touch the floor.

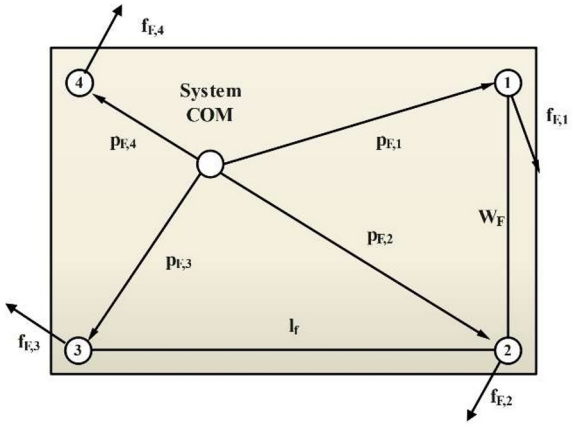

Fig. 3. Parameters for calculating forces for foot contact and effective length of frictional moment

p_{Q2C}^{Q} quadruped centroid's position with respect to the quadruped COM

μmgL_F The magnitude of this moment may be expressed as given in Equation (18), which encapsulates the geometrical characteristics of $\boldsymbol{p}_{F,i}$ and $\boldsymbol{f}_{F,i}$ in L_F [19].

In Eq (19) the proportion of the system weightage support at bottom i is denoted as $f_{C,i}$ Y [20]

$$\boldsymbol{p}_{F,i} = \boldsymbol{p}_Q + \boldsymbol{R}_Q\left(\boldsymbol{p}_{Q2C}^{Q} + x_{F,i}\boldsymbol{x} + y_{F,i}\boldsymbol{y}\right) - \boldsymbol{p}_{\mathrm{COM}}$$

$$x_{F,i} = \begin{cases} 0.5l_F & i = \{1,2\} \\ -0.5l_F & i = \{3,4\} \end{cases}, y_{F,i} = \begin{cases} 0.5w_F & i = \{1,4\} \\ -0.5w_F & i = \{2,3\} \end{cases} \quad (17)$$

$$\sum_{i=1}^{4} \|\tilde{\boldsymbol{p}}_{F,i}\boldsymbol{f}_{F,i}\| = \mu mgL_F \quad (18)$$

$$L_F = \sum_{i=1}^{4} f_{C,i}\|\boldsymbol{p}_{F,i}\| \quad (19)$$

3 Numerical Modeling and Trajectory Planning

What follows is an explanation of the mathematical model's Simulink implementation, the definition of an extra model for the multibody dynamics system, and the methodology for determining the trajectories of the tail joint angles. Due to the constraints of the stiction model, Simulink was selected to implement the system model. In order to activate static friction in the rotational stiction model, φ is adjusted to zero instead of changing sign. In Simulink, the "state port" option of the Integrator block permits pre-calculation of, φ, in order to determine if the sign would change. Instead of setting the integrator output to zero, the model does it if it would. To complement the Simulink model, we additionally construct a multibody dynamics model using MSC for the purpose of outcome comparison. The model takes advantage of the quadruped and tail models mass attributes and computer aided design geometry (Fig. 1(b)) to create the simulation parameters. Quadrupedal movement is computed after prescribing trajectories of tail joint angles and including contact friction models for all four feet [21]. The implementation of friction is a critical differentiator between Simulink and models. To simulate static friction, loading must first overcome it in the Simulink model's "pure" stiction model. However, the model incorporates a variable coefficient of friction that is influenced by the contact velocity between the ground and the foot, as seen in Figure 4.

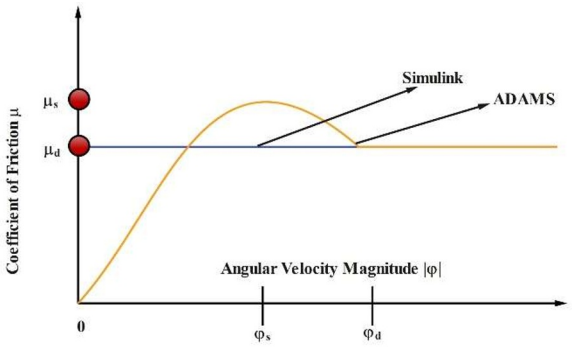

Fig. 4. Simulink profiles of friction coefficients for stiction and continuous models

As opposed to the friction coefficient, a discontinuity utilizes incessant stage functions: a middle-step from 0 to μ-s within the interval 0 to $\boldsymbol{\eta}$-s, and a complete-stepping from μ-s to μ-b within the interval θ-s to θ-d. The quad structural design has been employed and subsequently exported. The ankle, hip, and knee joints of the quadruped maintain a stationary position throughout the simulation. Following the generation of the tail trajectory in a MATLAB script, the angular velocity of the tail is represented by a spline. Under the appropriate initial angle condition, the tail is subjected to the specified angular velocity profile. By reducing the loading direction that induces undesirable rotation, the performance of the tail can be improved. The important of the joint acceleration is 0 when the tail is moved between two fixed places. But their relative magnitudes can be changed by adjusting the relative timespan of acceleration and deceleration. In order to command micro air vehicles, researchers have used split cycle frequency modulation to specify varying wing velocities for the up and down flaps [22]. The acceleration and deceleration of robotic tails could be achieved using this method.

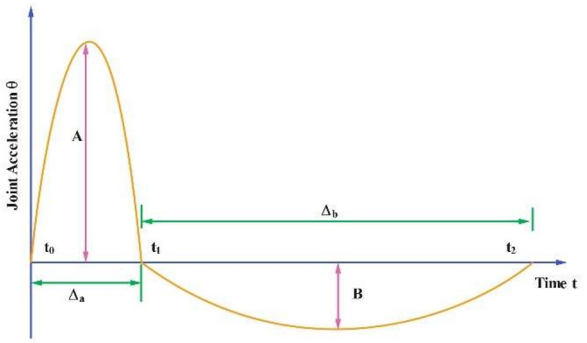

Fig. 5. Profile of split-cycle acceleration

In accordance with Equation (20), $\Delta_a = t_1 - t_0$ has a shorter acceleration duration and an extended deceleration duration of $\Delta_d = t_2 - t_1$. The combined angular accelerated outline is illustrated in Figure 5. A whole period ΔT and a split-cycle factor w_{ss} which can range from 0 to 1 are used to parameterize Δ_a and Δ_d in Equation (21).

$$\ddot{\theta} = \begin{cases} A\sin\left(\pi(t - t_0)/\Delta_a\right), & t_0 \le t \le t_1 \\ -B\sin\left(\pi(t - t_1)/\Delta_d\right), & t_1 < t \le t_2 \end{cases} \quad (20)$$

$$\Delta T = t_2 - t_0, \Delta_a = w_{ss}\Delta T, \Delta_d = \Delta T - \Delta_a \quad (21)$$

The equation (22) defines the boundary conditions for the tail trajectory, with θ_0 being the initial angle and $\Delta\theta$ being the angular displacement of the tail. The following equation shows the expressions for A and B that are obtained by integrating Eq. (20) using Eq. (22)

$$\theta(t_0) = \theta_0,\ \theta(t_2) = \theta_0 + \Delta\theta,\ \dot{\theta}(t_0) = \dot{\theta}(t_2) = 0 \quad (22)$$

$$A\Delta_a = B\Delta_d, A = \frac{\pi\Delta\theta}{w_{ss}(\Delta T)^2}, B = \frac{\pi\Delta\theta}{(1-w_{ss})(\Delta T)^2} \quad (23)$$

4 Case Study

In this part, the parameters for the simulation are defined, the mathematical model is compared to the multibody dynamics model, and how the tail structure and trajectory affect the net quadruped rotation, φ-net, is studied using the mathematical model. Table 1 shows the quadruped simulation parameters that were computed using the generic quadruped structure. The parts were defined as aluminum, and the friction parameters were estimated. Each 300 mm long and 2.4 kg tail has a variable number of connections between one and six. These values are established using the tail simulation parameters (Table 2). We compare the Simulink and ADAMS models to find out how different they are when it comes to modeling the quadruped system with a tail. We take into account two scenarios: a 1 and 6 DOF tail. In the 1DOF simulation with $\Delta\theta = -90$degrees and in the 6DOF simulation $\Delta\theta = -30$ degrees. The tail joint trajectory of each simulation is specified by $\Delta T = 0.25$, $\theta_0 =$ 0degrees and $w_{ss} = 0.25$ with $d_{Q2B} = 140.5$.

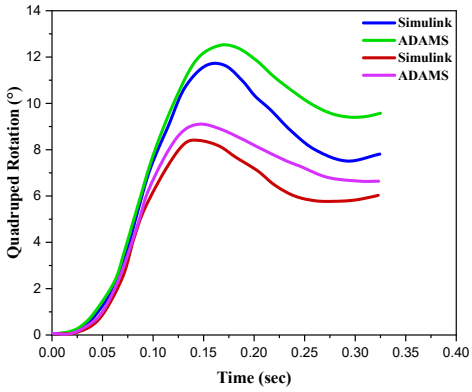

Fig. 6. Trajectories of the ADAMS and Simulink are compared

The findings are displayed in Figure 6. Because of the frictional modeling, the ADAMS model rotates more than the Simulink model in both instances. There is no friction in the ADAMS model when$\dot{\varphi} = 0$ and $\mu(\dot{\varphi}) = 0$. This makes the model more conducive to rotation, which in turn increases the anticipated rotation. The resultant quad rotating trajectory $\varphi(t)$ is displayed in Figure. 7 for a trajectory specified by $\Delta T = 0.25$, $\Delta\theta = -90\text{deg}, \theta_0 = 0\text{deg}$ and $w_{ss} = 0.25$ employing the 1DOF tail model. Figure 7 displays the related $M_{z,T}, M_{z,F}$, and $I_{zz}\ddot{\varphi}$ Key points along these trajectories are shown as A–D.

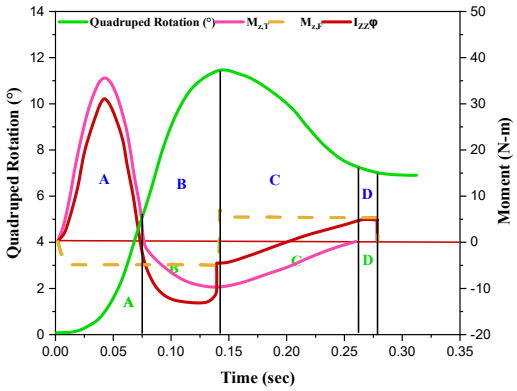

Fig. 7. The friction and associated tail and the u trajectory and the inertial moments for the 1DOF tail

After overcoming static friction with continuous dynamic friction resistance, as A, $M_{z,T}$ is positive we get φ. Nevertheless, as the phase comes to a close, the centripetal force of the tail causes $M_{z,T}$ to fall below zero. The element.is positive in B, but negative in $M_{z,T}$. The positive φ acts in opposition to both, M-z,T. and, M-z, F. until it reaches zero at the conclusion of B. As soon as, M-z, T. triumphs over static, M-z, F., the first. C becomes negative. During D, $M_{z,T}$ is equal to zero, but before, φ.=0, $M_{z,F}$ opposes the negative,φ. Two parameters d_{Q2B} and θ govern the tail's ability to transfer loading to the quad for a specific tail and quad. To demonstrate $M_{z,T}$ directly in terms of d_{Q2B} and θ, Eq. (24) expands Eq. (13) for the 1DOF tail.

$$M_{z,T} = -\left(I_{zz,L} + 0.25m_L L_L^2 \frac{m_Q}{m}\right)\ddot{\theta} + M_{z,T,\text{cen}} + M_{z,T,\tan}$$

$$M_{z,T,\tan} = I_{\text{eff}}\dot{\theta}^2 s_\theta I_{\text{eff}} = \frac{m_Q m_L}{2m} L_L d_{Q2B} \quad (24)$$

The $M_{z,T}$ moment comprises three components: (1) the moment of rotation, d_{Q2B}- and θ-invariant; (2) the moment of tangential acceleration caused by the tail; and (3) the moment of centripetal acceleration caused by the tail. Consequently, in accordance with the intended moment direction, the maximal joint velocities ought to favor θ=±90 degrees, while the joint acceleration should correspond to the intended direction, favoring θ=0 degrees.

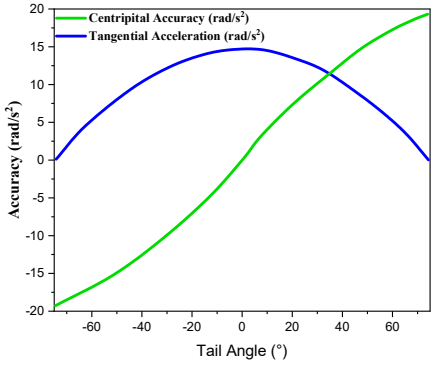

Fig. 8. An analysis of the centripetal and tangential contributions to ($\ddot{\varphi}$).

Considering the transmission's reliance on θ when in motion, the beginning angle θ_0 is crucial for a defined tail acceleration profile. It is required to have a tail trajectory with ΔT=0.25, $\Delta\theta$=−90deg, and w_{ss}=0.25 with

$\theta_0 \epsilon$[0deg,90deg] and $d\text{-}Q2B.\epsilon$ [0,0.15]m. The joint velocity/acceleration profiles are applied over multiple ranges of θ, although they remain constant by adjusting θ-0. The resultant,φ-net rotations for these simulation parameters are displayed in Figure 9, with, θ-0. And $d\text{-}Q2B$. being defined in 15deg and 0.025 m increments each.

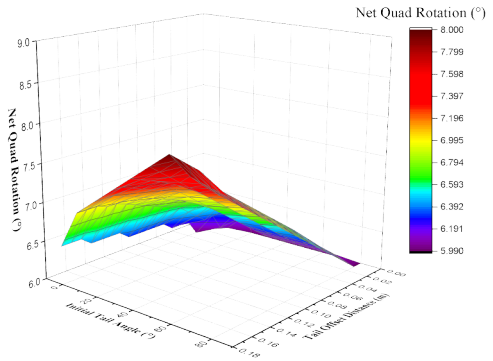

Fig. 9. Rotation of the net U as h0 and dQ2B vary

It is expected that as $d\text{-}Q2B$ increases, φ-net will also increase, because the tail forces are amplified over a longer duration. Based on the maximum, φ-net occurring mostly at, θ-0. =60deg, it may be inferred that, when considering the beginning angle, there is a little bias in favor of centripetal effects over tangential forces.

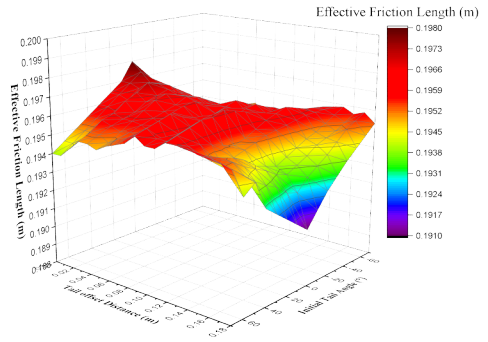

Fig. 10. Variations in LF for h and dQ2B

Furthermore, $L\text{-}F$ varies based on $d\text{-}Q2B$ and θ, as depicted in Figure 10. The highest deviation from the median of the range is < 3%, therefore variations in $L\text{-}F$ have minimal effect. An analysis of the split-cycle parameter's impact is performed using a tail trajectory that is described by ΔT=0.25 s, $\Delta\theta$=−90 deg, and, θ-0.=45 deg with $w_{ss}\epsilon$[0.1,0.9]. The result of varying, φ-net in increments of 0.1 from 0.1 to 0.9 is displayed in Figure 11. A higher net rotation is predicted by a lower w_{ss} The two main causes of this are (1) the widening gap between the magnitudes of angular acceleration in the desired and undesirable directions and (2) the bias in angular velocity in the θ>0 region. The highest speed is reached when $t = w_{\text{mod}}\Delta T$ and $\theta(w_{\text{mod}}\Delta T) = \theta_0 + w_{\text{mod}}\Delta\theta$. According to Eq. (24), the required moment owing to centripetal forces increases as the θ associated with the maximum velocity increases as w_{ss} is lowered.

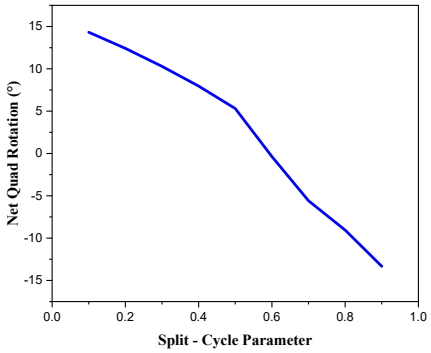

Fig. 11. Net $\boldsymbol{\varphi}$ rotation for varying $\boldsymbol{w_{ss}}$

For a given w_{ss} the maximum angular velocity of a tail is affected by two variables: $\Delta\theta$ and ΔT. To determine the effect of the maximum tail velocity, one uses a trajectory with the parameters w_{ss}.=0.25 and θ-0. =90 degrees, where $\Delta T\epsilon$[0.1,0.6] and $\Delta\theta\epsilon$[60deg,180deg] are employed. With ΔT and $\Delta\theta$ adjusted at 0.05 s and 30deg increments, Figure 12 shows the net φ rotation. The expected result is that. φ_{net} rises as $\Delta\theta$ increases and/or ΔT lowers.

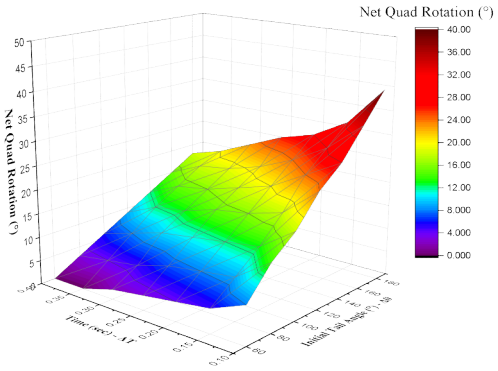

Fig. 12. Net $\boldsymbol{\varphi}$ rotation for varying $\boldsymbol{\Delta T}$ and $\boldsymbol{\Delta\theta}$

When thinking about the compromise between $\Delta\theta$ and ΔT, the centripetal acceleration becomes noticeable, as long as the maximum velocity of the tail $(2\Delta\theta/\Delta T)$ remains unchanged. The highest velocity is 10.47rad/s (600deg/s) as shown in Figure 13, for various values of $\Delta\theta$, with an associated ΔT. The increased tail motion at higher $\Delta\theta$ values is mainly due to the centripetal forces acting over a larger ΔT.

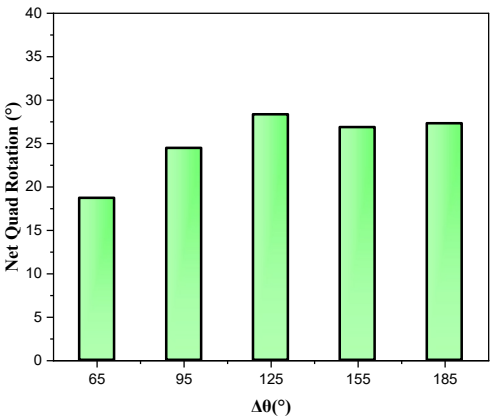

Fig. 13. A comparison of the net rotation of the tail at a constant maximal velocity

Selecting joint trajectories that permit a fair comparison is a significant difficulty when comparing tails with different degrees of freedom. In order to achieve this, we will impose two limitations on the tail trajectory: first, that it must move between the 2 extreme configurations within the allotted number of tail sections and second, that the maximum joint velocity for the respective trajectories of the joint angles must be the same. To suggest the velocity of maximal joint $|\dot{\theta}_{\max}|(10.47\text{rad/s}$ for these simulations), and the Equation (25) defines the $\Delta\theta$ and the ΔT variables [30].

$$\Delta\theta = -360\text{deg}/(n+1)\ \Delta T = 2\Delta\theta/|\dot{\theta}_{\max}| \quad (25)$$

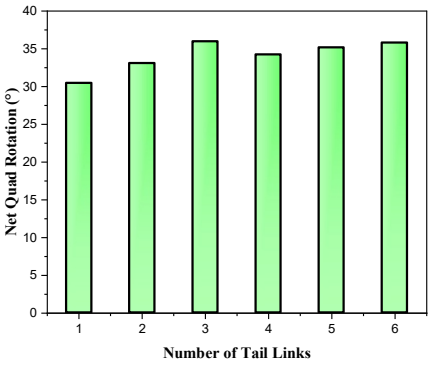

Fig. 14. Variable DOF tails' net $\boldsymbol{\varphi}$ rotation

As depicted in Figure 14, for a a-segment tail whose trajectories are denoted by ΔT and $\Delta\theta$ from Eq. (25), $\theta_0 = 0.5\Delta\theta$, and $w_{ss} = 0.25$. For a n-segment tail with trajectories given by ΔT and $\Delta\theta$ from Eq. (25), $\theta_0 = 0.5\Delta\theta$, and $w_{ss} = 0.25$ as shown in Figure 14. Once Eq. (4) is differentiated, it becomes clear that the angular acceleration of each connection incorporates the acceleration of its predecessors. As the trajectory progresses, the radial distance between the COMs of each link changes, causing the axial motion. At an angle of 30 degrees, the 6DOF tail's link 6COM is 209.4mm from the base frame, whereas at an angle of 0 degrees, the COM is 275 mm from the base frame.

5 Conclusions

The effect of the trajectory and geometry of a yaw-angle of plane robotic tail on the steering of quadrupeds was investigated in this study. Enhancing our mathematical and qualitative comprehension of the impact that tail-like devices onboard mobile robots have on their mobility has been the principal objective of this research. For trajectory planning, the centripetal and tangential inertial force loadings of the tail are roughly equivalent in significance, with the centripetal load being marginally more critical, according to the study. Additionally, it demonstrated the utility of split-cycle frequency modulation in regulating the relative magnitude of joint acceleration, as well as the advantages of multi-DOF tail structures. Both the designers and operators of future tail-assisted mobile robots will benefit from this work. For example, the optimal place to install the tail may be optimized, and for a certain design, the best trajectory to generate a desired yaw rotation can be determined.

References

1. J. Niu, H. Wang, H. Shi, D. Li, S. Li, S. Wu, Trajectory planning verification and gait analysis of wheel-legged hybrid robot with variable degree of freedom. Transactions of the Chinese Society of Agricultural Engineering, 33, (2017).
2. N.M.S. Pradhan, P. Frank, A. Mo, A. Badri-Sproewitz, Upside down: an open-source motion platform for highly dynamic movement, In ISR Europe 56th International Symposium on Robotics, (2023).
3. Wang Xiaolei, Jin Zhenlin, Li Xiaodan, Analysis and verification of terminal position error of leg parallel mechanism of quadruped robot. Transactions of the Chinese Society of Agricultural Engineering. 35, (2019).
4. F. Roscia, A. Cumerlotti, A. Del Prete, C. Semini, M. Focchi, Orientation control system: Enhancing aerial maneuvers for quadruped robots. Sensors. 23, (2023).
5. B. Luo, Balance control based on six-dimensional spatial mechanics and velocity adjustment through region intervention and foot landing for quadruped robot. Robotica. 40, (2022).
6. Nikkhah, H. Keshavarz, A. Yousefi-Koma, S.S. Mohtasebi, Design, dynamic modeling, and fabrication of a bio-inspired quadruped robot, In Third RSI International Conference on Robotics and Mechatronics, (ICROM), (2015).
7. W. Saab, P. Ben-Tzvi, Maneuverability and heading control of a quadruped robot utilizing tail dynamics, in ASME 2017 Dynamic Systems and Control Conference, (DSCC), (2017).
8. A.P. Sabelhaus, A.K. Akella, Z.A. Ahmad, V. SunSpiral, Model-predictive control of a flexible spine robot, In American control conference, (2017).
9. Jo, Hee-Heung, Gurbannazar Ishangulyyev, Jung-Yup Kim, Development and Motion Control of a Lightweight Robot Arm for Teleoperation Using VR Headset. Transactions of the Korean Society of Mechanical Engineers – A. (2023).
10. Y. Li, L. Cui, R. Song, C. Pang, Y. Li, A Scan Matching Method for Quadruped Robots in Outdoor Environment, In Second International Conference of Intelligent Robotic and Control Engineering, (IRCE), (2019).
11. W. Peng, Y. Zhiwei, Z. Cheng, D. Zhendong, Embedded control system design and experimental analysis of bionic quadruped robot, In the 26th Chinese Control and Decision Conference, (CCDC), (2014).
12. L. Li, Y. Fang, S. Guo, H. Qu, L. Wang, Type synthesis of a class of novel 3-DOF single-loop parallel leg mechanisms for walking robots, Mechanism and Machine Theory. 145, (2020).
13. T.K. Kumar, R. Kumar, S. Mogily, D. Goel, N. Pareekutty, S.V. Shah, K.M. Krishna, Implementation of gaits for achieving omnidirectional walking in a quadruped robot, In Proceedings of the Conference on Advances in Robotics, (2015).

14. X. Chen, F. Gao, C. Qi, X. Tian, Gait planning for a quadruped robot with one faulty actuator. Chinese Journal of Mechanical Engineering. 28, (2015).
15. J. Guo, Y. Zheng, D. Qu, R. Song, Y. Li, an algorithm of foot end trajectory tracking control for quadruped robot based on model predictive control. In IEEE International Conference on Robotics and Biomimetics (ROBIO), (2019).
16. X. Chu, S. Wang, R. Ng, C.Y. Fan, J. An, K.S. Au, Combining Tail and Reaction Wheel for Underactuated Spatial Reorientation in Robot Falling with Quadratic Programming. IEEE Robotics and Automation Letters. (2023).
17. J. Zhang, J. Shen, D.W. Hong, Kinematic Analysis and Design Optimization for a Reduced-DoF Quadruped Robot with Minimal Torque Requirements, In 17th International Conference on Ubiquitous Robots (UR), (2020).
18. H. Khan, M. D'Imperio, F. Cannella, D.G. Caldwell, A. Cuschieri, C. Semini, Towards scalable strain gauge-based joint torque sensors. Sensors. 17, (2017).
19. H. Yu, R. Sun, H. Nie, G. Qin, Design and Control of a Four-Link Mechanism for High Speed and Dynamic Locomotion, In International Conference on Intelligent Robotics and Applications, Berlin, Heidelberg, (2013).
20. G.Y. Ma, R.C. Liu, Y. Chen, J. Gao, P.B. Xu, Kinematics Analysis and Gait Planning of the Quadruped Robot Leg Mechanism. Transactions of Beijing institute of Technology. 40, (2020).
21. W. Rone, P. Ben-Tzvi, Dynamic Modeling and Simulation of a Yaw-Angle Quadruped Maneuvering with a Planar Robotic Tail. Journal of Dynamic Systems, Measurement and Control, Transactions of the ASME. 138, (2016).
22. L.G.D. de Barros, A.L.M. Cid, J.D. Domingues, V.S. Medeiros, G. Pessin, M. Becker, An Adaptable Paw Design for Quadruped Robots Operation in Mining Environments, In Latin American Robotics Symposium (LARS), (2023).
23. M. Bloesch, C. Gehring, P. Fankhauser, M. Hutter, M.A. Hoepflinger, R. Siegwart, State estimation for legged robots on unstable and slippery terrain. In IEEE/RSJ International Conference on Intelligent Robots and Systems, (2023).